

PAPER

# Geometrical optimisation of a personalised microneedle eye patch for transdermal delivery of anti-wrinkle small peptide

To cite this article: Seng Han Lim *et al* 2020 *Biofabrication* **12** 035003

View the [article online](#) for updates and enhancements.



**SUNP BIOTECH**

**BIOMAKER** EASY-TO-USE  
AFFORDABLE  
CUSTOMIZABLE  
FULLY FEATURED

BIOPRINTING.  
LIKE NEVER  
BEFORE.

LEARN  
MORE

# Biofabrication



## PAPER

# Geometrical optimisation of a personalised microneedle eye patch for transdermal delivery of anti-wrinkle small peptide

RECEIVED  
29 October 2019

REVISED  
23 December 2019

ACCEPTED FOR PUBLICATION  
17 January 2020

PUBLISHED  
8 April 2020

Seng Han Lim<sup>1</sup>, Wen Jun Tiew<sup>1</sup>, Junying Zhang<sup>2</sup>, Paul Chi-Lui Ho<sup>1</sup>, Nezamoddin N. Kachouie<sup>3</sup> and Lifeng Kang<sup>4,5</sup> 

<sup>1</sup> Department of Pharmacy, National University of Singapore, 18 Science Drive 4, Singapore 117543, Singapore

<sup>2</sup> Department of Pharmaceuticals of Traditional Chinese Medicine, China Pharmaceutical University, 24 Tong Jia Xiang, Nanjing, 210009, People's Republic of China

<sup>3</sup> Department of Mathematical Sciences, Florida Institute of Technology, 150 W. University Blvd., Melbourne, FL, United States of America

<sup>4</sup> School of Pharmacy, Faculty of Medicine and Health, University of Sydney, Pharmacy and Bank Building A15, Science Road, NSW 2006, Australia

<sup>5</sup> Author to whom any correspondence should be addressed.

E-mail: [lifeng.kang@sydney.edu.au](mailto:lifeng.kang@sydney.edu.au)

**Keywords:** 3D printing, microneedle, transdermal, anti-wrinkle, small peptide, material extrusion

Supplementary material for this article is available [online](#)

## Abstract

Acetyl-hexapeptide-3 (AHP-3) is a small peptide with good anti-wrinkle efficacy and safety profile. However, due to its hydrophilicity and high molecular weight, its skin permeation is generally poor. An innovative microneedle (MN) patch such as the curved, flexible or personalised MN patch is a viable avenue to deliver AHP-3. However, the well-researched geometrical relationship of MN on a flat MN patch cannot be assumed for these novel MN patches due to a complex mix of axial and shear forces. In this study, 3D printing was used for the fabrication of various MN patches with different MN geometries and curvatures. Both mechanical strength and skin penetration efficiency were used to determine the optimal MN geometry. The optimal MN geometry was then applied to the fabrication of a personalized MN patch (PMNP) for anti-wrinkle therapy, via 3D printing. In all, the general principles of MN geometrical effects on mechanical strength and skin penetration efficiency for a curved and a flat MN patch were similar. A MN height of 800  $\mu\text{m}$ , tip diameter of 100  $\mu\text{m}$ , interspacing of 800  $\mu\text{m}$  and base diameter of 400  $\mu\text{m}$  was observed to be the optimal MN geometry across all curvatures. *In vitro* skin permeation study demonstrated enhanced transdermal delivery of AHP-3 using the fabricated PMNP. Therefore, PMNP with optimized MN geometry can potentially be a novel approach to augment transdermal delivery of AHP-3 for effective wrinkle management.

## Introduction

The first indication of ageing often presents itself as folds or creases in the skin, or commonly known as wrinkles. These wrinkles are most commonly found in the periorbital region of the face [1, 2]. When an individual with wrinkles becomes excessively anxious over his/her facial outlook, several psychosocial issues can result, such as reduced ability to work or their self-esteem may take a plunge [3]. As such, to improve the psychosocial aspects of these individuals, simple and efficacious therapy for treating wrinkles is vital.

Acetyl-hexapeptide-3 (AHP-3) is a topically administered anti-wrinkle small peptide. Its main mode of

action involves inhibiting the release of a neurotransmitter, namely, acetylcholine. This inhibition results in a reduction of repeated contractions involving facial muscles that regulate facial expressions. This, in turn, decreases the formation of expression wrinkles. These wrinkles are creases or folds in the facial region due to repeated contractions of the same area [4–6]. Furthermore, AHP-3 is an attractive candidate for anti-wrinkle treatment due to its demonstrated efficacy, with a ~49% improvement of wrinkles after 4 weeks of a twice a day regime [4, 7, 8]. Compared to the more widely used Botulinum toxin (Botox<sup>®</sup>), AHP-3 also has a much favourable toxicity profile ( $\geq 2000 \text{ mgkg}^{-1}$ ) versus that of Botox<sup>®</sup>

(20 ngkg<sup>-1</sup>). In addition, the route of administration for Botox<sup>®</sup> is via an injection into the facial muscles at site of wrinkles [4], by a healthcare professional, as compared to the ability to self-administer AHP-3 in a cream or solution.

While AHP-3 appears to be a good candidate for anti-wrinkle treatment in terms of efficacy and safety, its skin permeation is often limited, due to a high molecular weight (889 Da) and a hydrophilic nature (logP value of -6.3) [8]. Only minimal amount of AHP-3 (0.01%) was delivered to the viable epidermis after topical application [9]. A huge amount of AHP-3 failed to permeate through the stratum corneum and remained on the skin surface. This inefficient drug delivery resulted in massive wastage and reduced efficacy due to insufficient drug concentration at site of action.

In view of this inefficient transdermal delivery, several groups have proposed various methods to improve the transdermal delivery of AHP-3. Most of these methods involved the optimisation of pharmaceutical formulations. For instance, using a high concentration of AHP-3 (10% w/w) in an oil-in-water emulsion, Kraeling *et al* demonstrated a modest improvement of skin permeation for AHP-3. However, the outcomes were still far from desirable as only 0.32% of AHP-3 managed to reach the viable epidermis [9]. Furthermore, the use of a high concentration can result in unwanted high cost of the final product. On the other hand, using a water-in-oil-in-water emulsion, Hoppel *et al* demonstrated a superior absorption of AHP-3 as compared to water-in-oil emulsion [10]. In similar formulation approach, Ruiz *et al* demonstrated superiority of a cream as compared to gel dosage form for the transdermal delivery of AHP-3 [11]. However, the increase in AHP-3 delivered to the viable epidermis, was once again, modest. More recently, using various molecular modification of the chemical structure, Lim *et al* demonstrated a significant enhancement of transdermal delivery of AHP-3 analogues, as compared to AHP-3 [12]. However, this method brings about concern of efficacy and safety for the newly modified compounds. Therefore, there is a need for improvements to AHP-3 transdermal delivery which may enhance its action and greatly benefit individuals plagued by periorbital wrinkles.

The use of microneedle (MN) assisted transdermal drug delivery system provides a feasible avenue to enhance skin permeation of AHP-3, via micro-pores/channels created by MNs [13]. Moreover, MN has the benefit of a localised action with minimal systemic side effects. MN usage also allows ease of self-administration without significant pain (due to its minimally invasive nature). This could potentially improve patient compliance [11, 13–15] which is critical for improved patient outcomes. In the past few decades, extensive research on MNs was conducted to optimise transdermal drug delivery [16]. However, most studies were carried out for flat MN patch, which has been

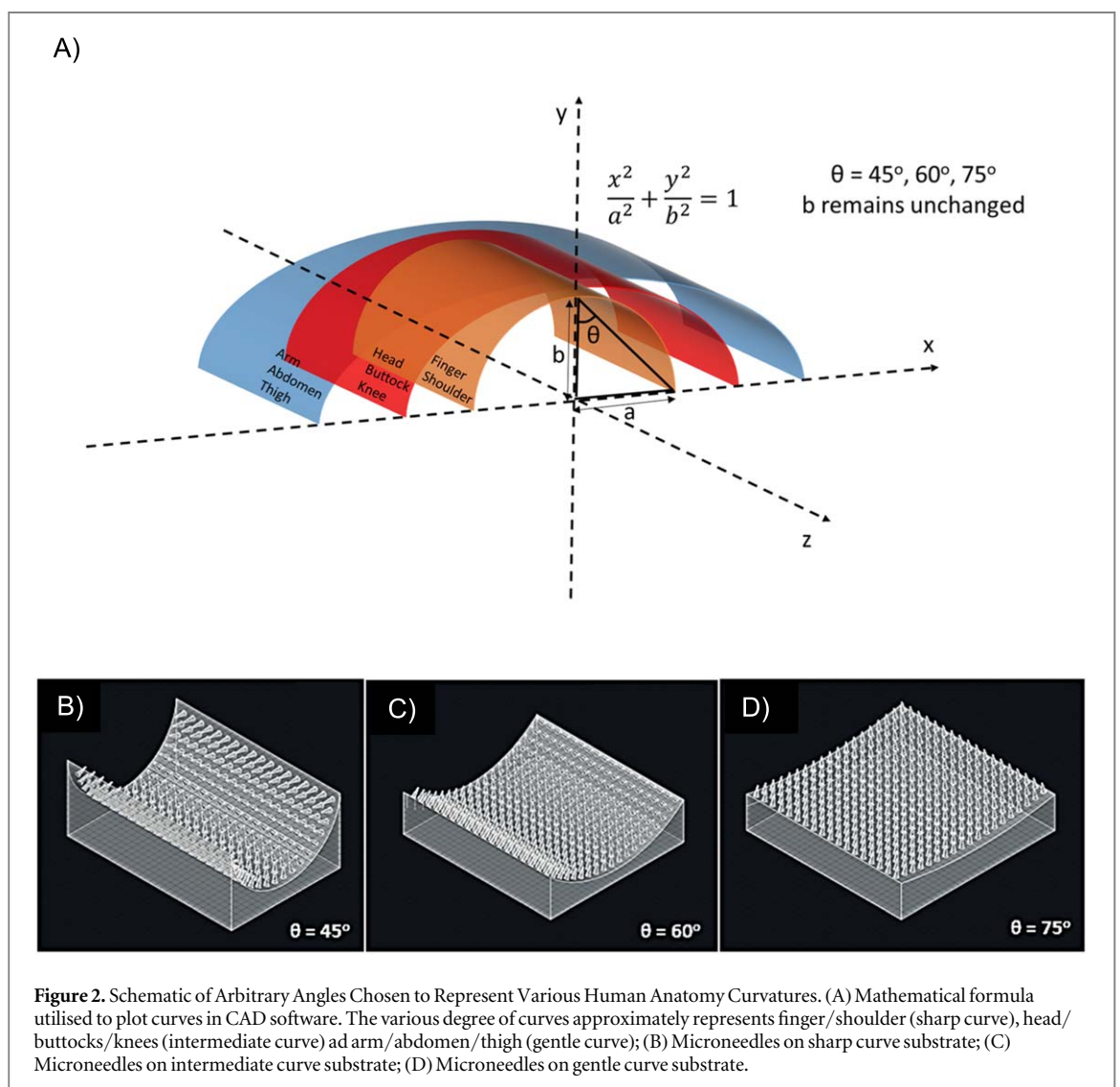
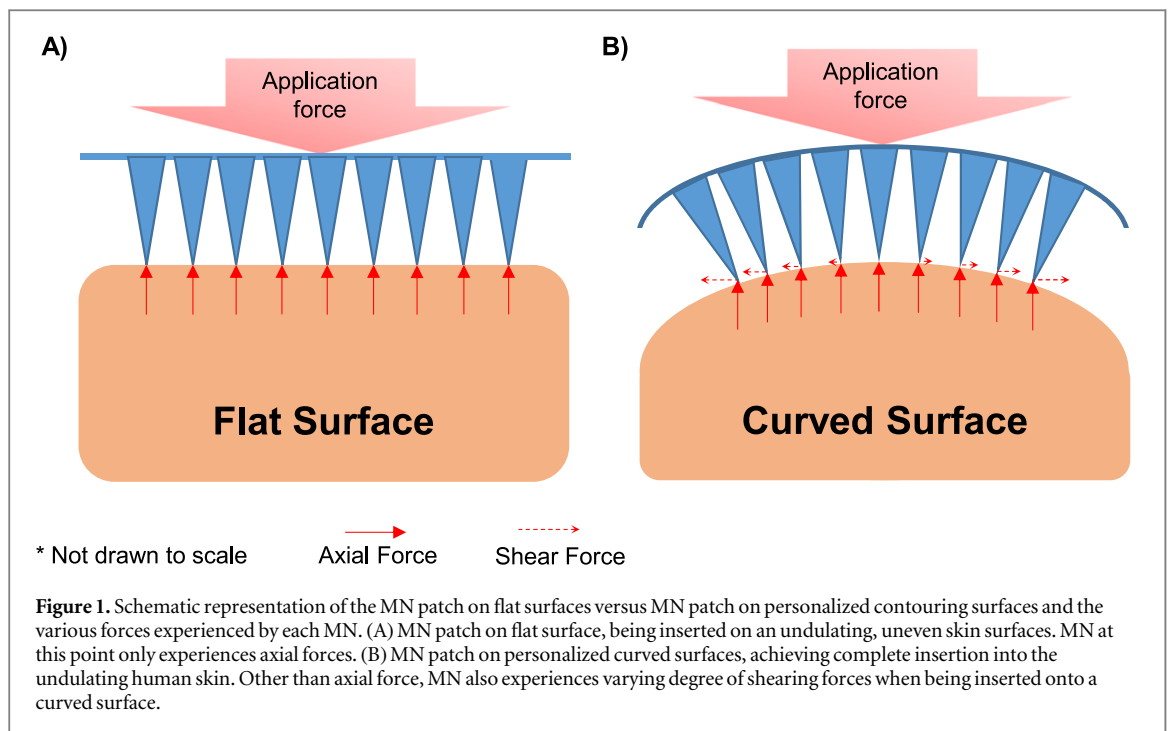
seen in recent years, as inadequate for efficient application to the undulating and elastic human skin surfaces [17, 18]. Flat MN patch is subjected to a ‘bed of nails’ effect, which causes non-uniform insertion of MNs on an undulating skin surface [19]. Hence, this leads to non-uniform dosing which may affect treatment outcomes and increased risk of MN breakage due to unbalanced resistant forces [20, 21]. Intuitively, curved [22], flexible [23, 24] or personalised [19] MN patches would conform well to uneven body surfaces. However, the fabrication of curved MN is often tedious and the correct use of flexible MN is dependent on user expertise to ensure proper fit. Therefore, a PMNP that contours to the periorbital region in a fixed shape, will be of great potential for transdermal delivery of AHP-3 in the treatment of periorbital wrinkles.

However, in the development of a PMNP, it cannot be assumed that any MN geometrical relationships drawn from flat MN patch can be directly applied to curved MN patch. As illustrated in figure 1, while only axial forces are experienced in a flat MN patch, a complex mix of axial and shear forces are experienced by curved or personalised MN patch. Therefore, this study aims to first, optimise the MN geometry for varying curvatures of MN patch, and second, to fabricate a PMNP with an optimised MN geometry for the periorbital region. 3D scanning and 3D printing via digital light processing (DLP), with the aid of computer-aided design (CAD) software, were employed to create polymeric MN patches with varying curvatures and MN geometries required for the study. This method of additive manufacturing is chosen due to its ability to construct complex structures rapidly and precisely, unlike traditional subtractive or formative manufacturing [25–28].

## Materials and methods

### Materials

The 3DM-castable resin was purchased from 3D-Materials SASU (Feldkirch, France). AHP-3 was received from Kaijie Peptide Company (Sichuan, China). Sulforhodamine B, phosphate buffered saline (PBS) and calcein disodium dye were purchased from Sigma-Aldrich (Merck KGaA, Darmstadt, Germany). All mentions of water refers to deionised, grade 1 water filtered from a laboratory water purification system (Adrona Crystal, Latvia), unless otherwise stated. Polydimethylsiloxane (PDMS) (Sylgard 184 Silicone Elastomer Kit) was obtained from Dow Corning (Midland, MI, USA). PrestoBlue<sup>®</sup> was obtained from Invitrogen (Carlsbad, CA, USA). Culture media consisted of Dulbecco’s Modified Eagle Medium (DMEM) (Invitrogen) supplemented with 10% of fetal bovine serum (FBS) (Invitrogen) and 1% of 10 000 U ml<sup>-1</sup> penicillin and 10 mg ml<sup>-1</sup> streptomycin (PS) (PAN-Biotech GmbH, Germany). Porcine cadaver skin was obtained from NUS Animal Centre, approved by NUS Institutional Animal Care and Use Committee



(IACUC). Human dermatome cadaver skin was obtained from Science Care (Arizona, USA). The skin tissues were excised from a 66 years old Caucasian female and the use of these skin tissues were approved by NUS Institutional Review Board (IRB). 10% neutral buffered formalin was purchased from Leica Biosystems Nussloch GmbH (Germany). All other reagents were of analytical grade.

### Design of curved MN patches for MN geometry optimisation

AutoCAD<sup>®</sup> 2017 (Autodesk<sup>®</sup> Inc., San Rafael, CA, USA) was used for the design of curved MN patch (CMNP) that were first used for optimisation of MN geometry. Three varying curvatures of MN patch were studied, namely sharp ( $\theta = 45^\circ$ ), intermediate ( $\theta = 60^\circ$ ) and gentle ( $\theta = 75^\circ$ ), as illustrated in figure 2. Three parameters of MN geometry were also investigated, namely MN height (or length), tip diameter and interspacing (centre-to-centre spacing). A reference model and base diameter of 400  $\mu\text{m}$  were used as baselines in determining the MN geometries, with the choices of aspect ratios guided by previous studies [24–26]. The surface area of all CMNP models was kept constant at 2.25  $\text{cm}^2$  for purpose of comparison in subsequent experiments. This was achieved by reducing the length of  $b$  as appropriate, while keeping the same  $\theta$  as per previously determined.

### Fabrication of MN patches

A Digital Light Processing (DLP) 3D printer (Titan 2HR, Kudo3D Inc., CA, USA), assembled with Optoma<sup>®</sup> DLP projector, was employed to fabricate the CMNPs. The designed CMNP CAD models were exported from AutoCAD<sup>®</sup> in .STL format and digitally sliced into 25  $\mu\text{m}$  layers via Creation Workshop Envision Labs (St. Mankato, MN, USA) to give individual two dimensional (2D) images. Following which, these images were compressed into a .zip file and processed in Titan 2HR's control software to initiate printing. The XY resolution of the Titan DLP printer was set as 37  $\mu\text{m}$  and the resin used for 3D printing was 3DM-Castable resin. The print settings were optimised from the guide supplied by Kudo3D Inc. [29]. The parameters optimised included lifting speed, lifting height, exposure time and the time delay before next exposure. Briefly, the DLP 3D printer function based on the principles of vat polymerisation. Once the build platform is lowered into the resin and comes into contact with the bottom of the resin container, the DLP projector projects a 2D image onto the resin container, as per determined by the individual image slices previously, and polymerises a thin layer of liquid resin into a solid. The build platform then separates from the resin container at the pre-optimised speed and height to allow fresh uncured resin to flow into the area below the printed parts and

the build platform. This process repeats, until the entire object is printed.

### Post-fabrication treatment

The printed CMNPs were detached from the build platform of 3D printer using a sharp blade and subjected to post-fabrication processes modified from Oskui *et al* [30]. Firstly, the CMNPs were soaked in isopropyl alcohol (IPA) to eliminate any residual resin from the surface of the printed parts. A fresh change of IPA was made every 15 min until no obvious colouration was observed in IPA. Excess amount of IPA on the printed parts was rinsed off using tap water and the CMNPs were left to dry. Subsequently, the CMNPs were exposed to UV-visible radiation at 400 nm under an enclosed LED lamp for 2 h to polymerise any remaining uncured resin. Thereafter, the CMNPs were soaked sequentially in 1X PBS for 24 h followed by 70% v/v ethanol for another 24 h. The final CMNPs were left to dry in ambient room temperature and pressure before use [19]. This series of treatment had been demonstrated to render the final product biocompatible with human dermal cell lines [19].

### Mechanical strength testing for CMNP

The CMNPs were first photographed with a Nikon SMZ-25 stereomicroscope (Nikon, Japan) and the Nikon imaging software (NIS-Element Analysis D 4.20.00) to obtain the pre-compression images. Next, Algol JSV H1000 digital force gauge (Algol Instrument Co. Ltd Taiwan) was employed to compress the CMNPs against curved acrylonitrile butadiene styrene (ABS) substrates corresponding to the three curvatures, at 40 N for 30 s. The curved ABS substrates were fabricated via Fused Deposition Modelling 3D printer, Da Vinci 1.0 (XYZ printing Inc., CA, USA). Subsequently, the CMNPs were photographed with the same stereomicroscope to obtain the post-compression images. The 'pre' and 'post' images were visually compared to identify MN fractures and determine the percentage of intact MNs. A triplicate was conducted for each combination of curvature and its geometry [12, 19, 25, 31, 32].

### Skin penetration efficiency testing for CMNP

Curved polydimethylsiloxane (PDMS) substrates, which mimic full-thickness skin, were prepared in advance. Briefly, a mixture of silicone elastomer base and curing agent in a weight to weight ratio of 9:1 was poured into the reverse moulds (3D printed via Titan 2HR, Kudo3D Inc., CA, USA) corresponding to the three curvatures. The elastomeric mixture was then degassed in a vacuum chamber to remove entrapped air bubbles, prior to heat curing at 70 °C for 2 h to obtain the hardened PDMS substrates [19, 27, 31]. CMNPs were dip-coated with fluorescent dye sulforhodamine B [33] and left to stand for 10 min while protected from light. The excess dye was drained off

using Kimwipes™. Thereafter, porcine cadaver skin was laid stretched over a curved PDMS substrate with epidermis side facing up and the dip-coated CMNP was compressed onto the skin using a thumb (~20 N) [34] in a slow rotational motion for 30 s. Excess dye on the skin was wiped off using 70%v/v ethanol. Subsequently, the stained porcine skin was visualized with fluorescence illumination, using the Nikon SMZ-25 stereomicroscope to identify the extent of penetration. The percent penetration was determined by counting the number of stained holes, which represents stratum corneum perforation, as a percentage of the total number of MNs. Triplicates were performed for this test [19, 27].

### ***In vitro* biocompatibility of fabrication CMNP**

Based on EN ISO 10993-12:2012 guidelines, the *in vitro* biocompatibility of fabrication CMNP was conducted using three 1 cm<sup>3</sup> cubes previously printed and post processed. The cubes were subsequently soaked in 6 ml of PBS for 24 h.

Human dermal fibroblast (HDF) and human adult low calcium high temperature (HaCaT) cells were used to assess the toxicity of the 3D printing resin. Cells were grown in DMEM supplemented by 10% FBS and 1% penicillin–streptomycin solution. 10 000 cells were plated into 96-well microtiter plates with 200  $\mu$ l of culture medium in each well. After 24 h of incubation at 37 °C and 5% CO<sub>2</sub>, all culture medium was removed and replenished with 180  $\mu$ l of fresh culture medium plus 20  $\mu$ l of polymer extract for each well. The negative control consisted of cells incubated with 180  $\mu$ l of fresh culture medium and 20  $\mu$ l of sterile PBS. The plates were incubated at 37 °C and 5% CO<sub>2</sub> for 24 h (1 Day) and 72 h (3 Days).

At the end of Day 1 and Day 3, 22  $\mu$ l of PrestoBlue<sup>®</sup> cell viability reagent was pipetted into each of the wells. The 96-well plate was then incubated for 30 min under the same incubation conditions stated above. The absorbance of each well was then analysed with an absorbance plate reader (SpectraMax<sup>®</sup> 190, Sunnyvale, CA, USA) at a wavelength of 570 nm and a reference wavelength of 600 nm.

The normalized background absorbance of resorfin was determined from the blanks and subtracted from the normalized absorbance of the experimental and standard reference wells to obtain the corrected absorbance. Subsequently, the corrected absorbance of the experimental wells was expressed as a percentage of the negative control to determine the relative cell viability.

### **Statistical model for prediction of optimal microneedle geometry**

We design a logistic regression to model the MN mechanical strength with regard to microneedle geometry. In the proposed model, the percentage of MN that are intact is considered as response variable

and microneedle curvature, interspacing, length, and tip diameter are considered as factors. Several experiments were performed to collect data for response and factors. In each experiment a specific combination of these factors was selected and the percentage of MN that were intact was calculated at the end of each experiment.

Overall, 81 experiments for different combinations of MN parameters (MN curvature or ‘MNC’, MN interspacing or ‘MNI’, MN length or ‘MNL’, MN tip diameter or ‘MNT’) were implemented and completed. The parameters of MNC were set to 45°, 60°, and 75° and the parameters of MNI were set to 400, 800, and 1200  $\mu$ m. MNL were set to 400, 800, and 1200  $\mu$ m and the MNT of selected needles were 50, 100, and 200  $\mu$ m. A minimum of 42.1% of micro-needles were intact for the combination of (MNC: 60°, MNI: 800  $\mu$ m, MNL: 1200  $\mu$ m, MNT: 100  $\mu$ m) and a maximum of 98.6% were intact for the combination of (MNC: 75°, MNI: 800  $\mu$ m, MNL: 400  $\mu$ m, MNT: 100  $\mu$ m).

In the next step, we performed cluster analysis to identify the MN geometry with optimal MN mechanical strength. To this end, we constructed a feature vector (FV) = [curvature, interspacing, length, tip diameter, mechanical strength] for each experiment and applied K-means clustering to divide the feature vectors to four clusters and discover the MN geometry for optimal MN mechanical strength.

### **3D scan of human volunteer**

3D scanning of the face of a human volunteer (30-year-old, Chinese, male) was performed with a commercial scanner (Artec Eva, Artec3D, Luxembourg) at a distance of ~50 cm away from the human volunteer in accordance with the manufacturer’s recommendations. The 3D scanner was panned 360° around the head of the volunteer to capture a 3D image that was exported directly to the corresponding software Artec Studio 11 (Artec3D, Luxembourg) for processing. The final CAD model of the human volunteer face was saved and subsequently processed using a suite of programme including Fusion 360 (Autodesk<sup>®</sup> Inc., San Rafael, CA, USA), Remake (Autodesk<sup>®</sup> Inc., San Rafael, CA, USA) to convert it into a solid model which can be imported into Solidworks<sup>®</sup> 2016 (Dassault Systemes, France).

### **Design & fabrication of PMNP**

The human face CAD model was processed using Solidworks<sup>®</sup> 2016 (Dassault Systemes, France). A personalised eye patch was designed to fit snugly to the contours and dimensions of the face CAD model. Subsequently, arrays of MNs were created on the patch’s inner contoured surface. The MNs were designed to have 400  $\mu$ m base diameter, 800  $\mu$ m centre-to-centre spacing. The MN height was set at 800  $\mu$ m and with a tip diameter of 100  $\mu$ m. These

dimensions were derived from the best performing MN geometrical combination for mechanical strength and skin penetration efficiency. The completed CAD model was exported as .STL file and 3D printed in a same way as described previously.

#### **Preparation of human cadaver skin prior to use**

Human cadaver dermatomed skin, after excision, were stored in  $-80^{\circ}\text{C}$  freezer until use. Skin samples were hydrated in water. All skin used were measured for the electrical resistance using an electrical resistance meter (LCR-916, GW Instek, Good Will Instrument Co. Ltd, Taiwan) prior to use (before *in vitro* skin permeation or any penetration studies). Based on internal lab standards, human cadaver dermatomed skin needs to have a minimum electrical resistance of 1 kV at 1 kHz in 1X PBS solution, before it is considered as intact with a complete skin barrier. Any skin samples with electrical resistance below 1 kV were not used.

#### **Histological examination of human cadaver skin**

Personalised PDMS substrates based on the human face CAD model, to mimic full-thickness skin, were prepared in advance, using a 3D printed reverse mould fabricated by an FDM printer (CEL Robox<sup>®</sup>, England, UK). Thereafter, dermatomed human cadaver skin was laid stretched over the personalised PDMS substrate with epidermis facing up and PMNP was compressed onto the skin using a thumb ( $\sim 20\text{ N}$ ) in a slow rotational motion for 30 s. The PMNP treated skin samples were fixed with 10% neutral buffered formalin for 48 h and subsequently transferred to 15% sucrose solution 24 h before sectioning. Immediately before sectioning, the skin samples were frozen in the embedding matrix using liquid nitrogen for deep freeze. The skin samples were then separately cross-sectioned using the cryostat (CM3050 S, Leica, Germany) to obtain cross-sectional slices of  $10\ \mu\text{m}$  thick. The cross-sections were stained using standard protocols of hematoxylin and eosin (H&E) staining. The obtained stained samples were imaged and analysed using the Nikon SMZ25 stereomicroscope for the depth of punctured pores. These steps were repeated for the histological section of samples punctured using a commercial, flexible MN patch (FMNP) (NaVision<sup>™</sup>, Shiseido, Tokyo Japan) [35] to treat the human cadaver skin and also for intact human cadaver skin.

#### ***In vitro* skin permeation of calcein dye for human cadaver skin**

Personalised PDMS substrates as described in section 2.9 were used for this experiment. Dermatomed human cadaver skin was laid stretched over the personalised PDMS substrate with epidermis facing up and PMNP was compressed onto the skin using a thumb ( $\sim 20\text{ N}$ ) in a slow rotational motion for 30 s.

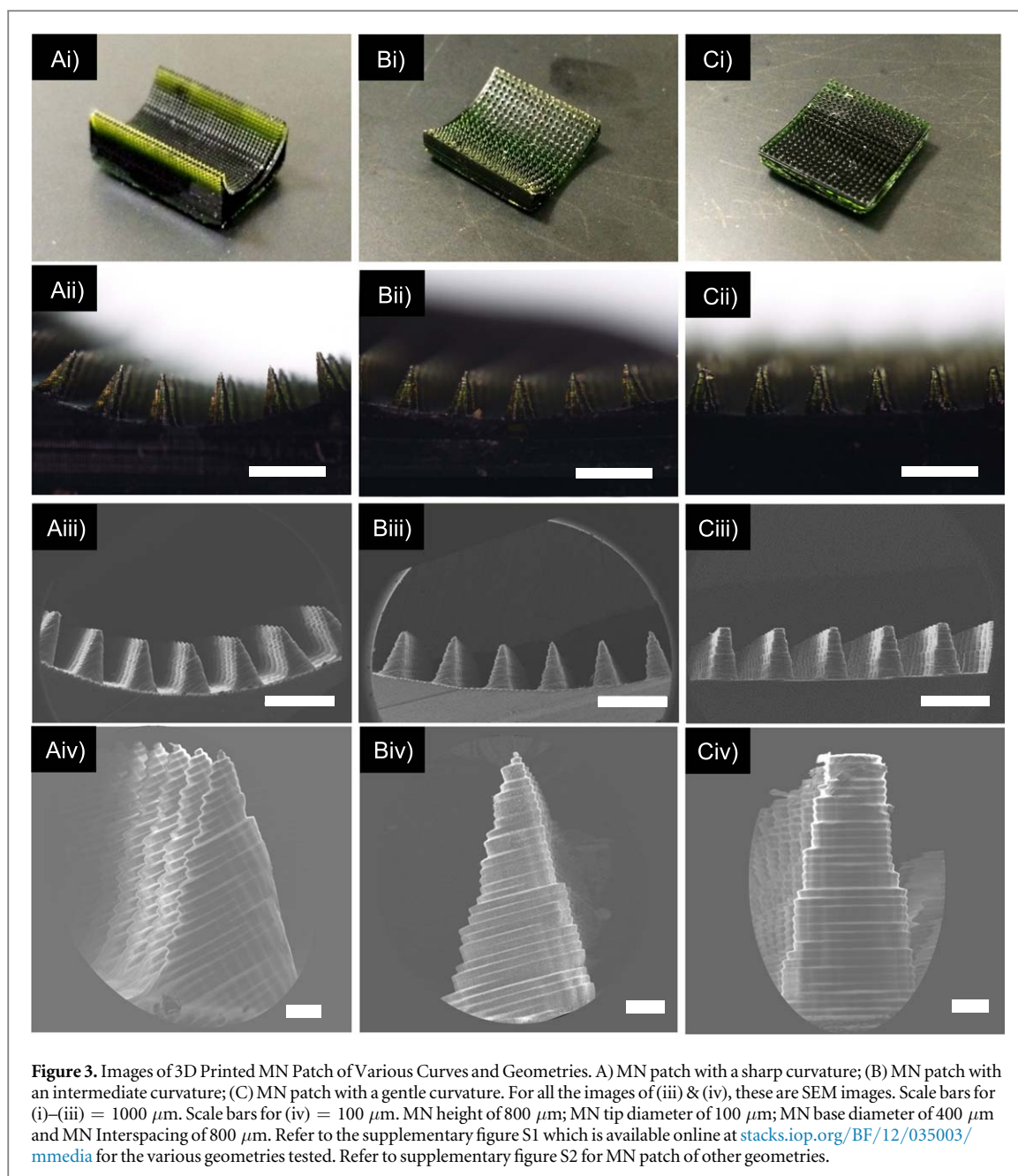
Thereafter, PMNP treated skin sample was transferred to a vertical Franz diffusion cell with an effective exposed area of  $1\text{ cm}^2$ .  $500\ \mu\text{l}$  of calcein disodium solution (50 mM) in water with an excitation/emission wavelength of 495/515 nm, was added to the donor cell and 4.8 ml of PBS was added to the receptor cell. The cells were placed inside a hot air chamber maintained at  $32^{\circ}\text{C}$  with magnetic stirring at 180 rpm. The temperature of  $32^{\circ}\text{C}$  was chosen to simulate the surface temperature of human skin on the body and has been commonly used in other skin permeation studies [6, 19]. At the end of 18 h, skin samples were removed from the cell and rinsed with water and dried using Kimwipes<sup>™</sup>. Finally, the depth of permeation and relative amount of Calcein AM within the skin were observed under a confocal microscope (FV 1000 TIRF, Olympus, Tokyo, Japan). This experiment was repeated with FMNP treated human cadaver skin and intact human cadaver skin.

#### ***In vitro* skin permeation of AHP-3 for human cadaver skin**

The procedure as described in section 2.12 were used in this experiment, except for the use of  $500\ \mu\text{l}$  of 10% w/v AHP-3, instead of calcein disodium, in the donor cell. The receptor solution was subjected to high performance liquid chromatography (HPLC) analysis of AHP-3 permeated through skin, at time points of 0.5, 1, 3, 6, 9, 21, 24 h. The entire receptor solution was withdrawn at each time point and replaced with fresh receptor solution. The receptor solution in this case was freshly prepared 1X PBS. Triplicates were performed for each set of experiment [19, 25]. At the end of 24 h, skin samples were removed from the diffusion cell and processed to analyse the amount of AHP-3 within the skin. The procedures were repeated for that of intact human cadaver skin, FMNP treated human cadaver skin and a commercial AHP-3 transdermal patch treated human cadaver skin.

#### **Extraction of AHP-3 from human cadaver dermatomed skin**

At the end of 24 h *in vitro* skin permeation, the skin samples were removed from the Franz diffusion cell. The epidermal surface was gently rinsed with water to wash off any residual AHP-3 solution not permeated. Thereafter, the skin was homogenised using a pestle and mortar with 1 ml of water added into the mortar. Once the skin samples were sufficiently homogenised, the skin samples were transferred into a 15 ml falcon tube and an additional 3 ml of water was added to the tube for extraction of AHP-3 from the skin. The tube was maintained at  $4^{\circ}\text{C}$  and left for 24 h for extraction of AHP-3 to occur. At the end of extraction, the tube was centrifuged at high speed of 10 000 rpm for 3 min (Rotina 35R, Hettich, Tuttlingen, Germany) to remove



any skin samples and the supernatant was analysed for the contents of AHP-3.

#### Drug analysis

The quantity of AHP-3 was determined using Shimadzu LC-20AD HPLC machine with SDP-M20A UV detector. The column used was an Agilent Zorbax Eclipse Plus C18 column (3 mm  $\times$  150 mm  $\times$  5  $\mu\text{m}$ , 95  $\text{\AA}$ ). The mobile phase consisted of mobile phase A (0.1% v/v trifluoroacetic acid in water) and mobile phase B (0.1% v/v trifluoroacetic acid in acetonitrile) with an isocratic elution program. The ratios of mobile phase solvents A:B was 9:1. The flow rate was set at 1 ml·min<sup>-1</sup> with an injection volume of 20  $\mu\text{l}$  for each sampling and UV detection was executed at a

wavelength of 215 nm. A standard calibration curve was plotted using the respective standard solutions from 1 to 500 ppm.

#### Statistical/data analysis

All data were analysed and arranged using GraphPad Prism 6 (GraphPad Software Inc., CA, USA) for any graphical outputs. All individual tests were conducted in triplicates and the results were presented as mean  $\pm$  standard deviation. Statistical analysis was performed by one-way analysis of variance followed by Tukey *post hoc* test using IBM SPSS Statistics 21.0 (IBM, New York, USA). A probability value of  $p < 0.05$  was considered statistically significant.

## Results

### Design and fabrication of CMNP

A matrix of CMNP with varying curvatures and MN geometries were fabricated using a DLP 3D printer. Optimization of print settings such as exposure time, lift speed and lift height were performed to ensure good accuracy and precise fabrication of CMNPs. The printed CMNPs have a total surface area of  $2.25 \text{ cm}^2$  to allow for subsequent comparison between the CMNPs on their mechanical strength and skin penetration efficiency. Representative images of the CMNP of varying curvatures are illustrated in figure 3. The MN illustrated here are that of MN height  $800 \mu\text{m}$ ; MN tip diameter  $100 \mu\text{m}$ ; MN base diameter of  $400 \mu\text{m}$  and MN interspacing of  $800 \mu\text{m}$ .

### Mechanical strength testing for CMNP

A higher percentage of MN remaining intact, after compression at 40 N for 30 s, will indicate higher mechanical strength. Average thumb force, of 20 N for 30 s [34], was used to penetrate the skin subsequently. Therefore, a force of 40 N was chosen for mechanical strength testing to account for potential breakages in MN due to handling and penetration. Consistently across all curvatures, mechanical strength of CMNP decreases with increasing length from 400 to  $1200 \mu\text{m}$ . Similar trend of decreasing mechanical strength was observed with decreasing tip diameter from 200 to  $50 \mu\text{m}$  and with increasing interspacing from 400 to  $1200 \mu\text{m}$ , as depicted in figure 4A. The percentage of intact MN after compression of CMNPs ranged from 48%–98% across all curvatures. Specifically, for MN length of  $400 \mu\text{m}$  and  $800 \mu\text{m}$ , all tip diameters and interspacing of  $400 \mu\text{m}$  and  $800 \mu\text{m}$  exhibited high mechanical strength with percentage of intact MN exceeding 80%. Contrastingly, length and interspacing of  $1200 \mu\text{m}$  showed poor mechanical strength with percentage of intact MN below 80%. The results showed that there was no difference in mechanical strength between length of  $400 \mu\text{m}$  and  $800 \mu\text{m}$  for all curvatures, except for gentle curvature. Generally, there were no statistical differences in mechanical strength between tip diameters for all curvatures, except for between  $50 \mu\text{m}$  and  $100 \mu\text{m}$  or  $200 \mu\text{m}$  in the gentle curvature. Also, there was no statistical difference in mechanical strength between interspacing of  $400 \mu\text{m}$  and  $800 \mu\text{m}$  across all curvatures. Therefore, these results reflected that MNs fabricated via this 3D printing method were generally able to withstand breakage from a typical thumb force of  $\sim 20 \text{ N}$  which was applied for subsequent skin penetration studies, except for length and interspacing of  $1200 \mu\text{m}$ .

### Skin penetration efficiency for CMNP

A larger number of micro-pores created after MN application correlates with higher skin penetration

efficiency and potentially better transdermal drug delivery. Figure 4(B) illustrated the percentage penetration of CMNP. This ranged from 43%–93% across all curvatures, with MN length of  $800 \mu\text{m}$ , tip diameter of  $100 \mu\text{m}$  and interspacing of  $1200 \mu\text{m}$  possessing higher skin penetrating power beyond 70%. In general, statistical analysis of the results demonstrated a significant difference in skin penetration efficiency of different MN length within each curvature, except for the comparison between  $800 \mu\text{m}$  and  $1200 \mu\text{m}$  MN length of the sharp curvature. On the other hand, statistical differences in skin penetration were absent amongst tip diameters within each curvature, except for the comparison between  $200 \mu\text{m}$  and  $50 \mu\text{m}$ ;  $200 \mu\text{m}$  and  $100 \mu\text{m}$  with a gentle curvature. Also, there was no statistical difference in skin penetration efficiency between interspacing of  $800 \mu\text{m}$  and  $1200 \mu\text{m}$  across all curvatures. Surprisingly, it was observed that skin penetration efficiency was the highest for most MN geometries of the intermediate curvature, apart from interspacing of  $400 \mu\text{m}$  whereby gentle curvature was superior. Comparatively, CMNP with higher mechanical strength generally resulted in weaker skin penetration for most MN geometries, excluding length of  $1200 \mu\text{m}$  which demonstrated relatively good penetration despite poor mechanical strength.

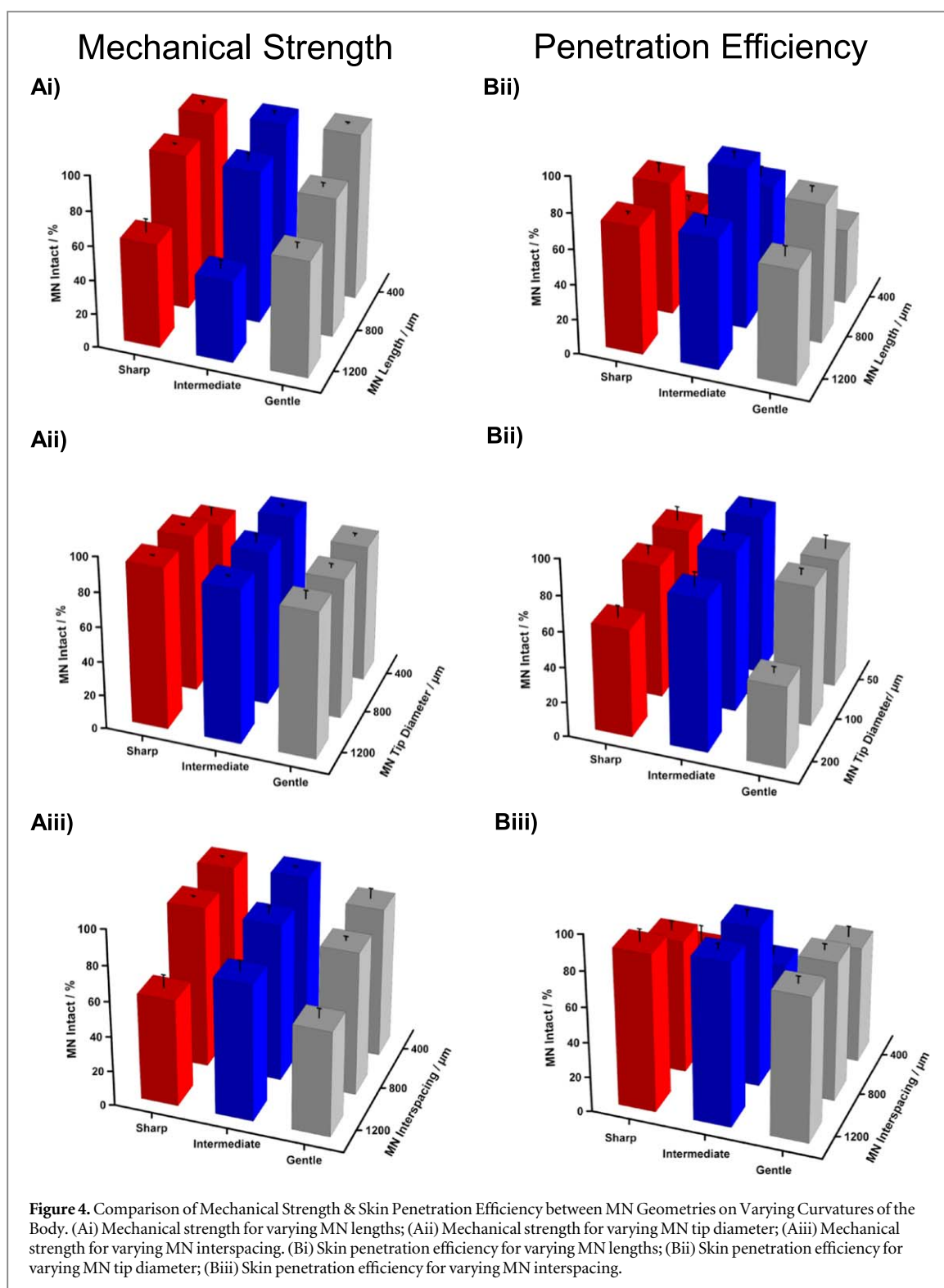
### *In vitro* biocompatibility of fabrication CMNP

A relative cell viability of more than 100% (figure 5) was observed for both HDF and HaCaT cells for up to 72 h of incubation with the 3D printing material extract, as compared to the negative control of the same type of cells. It indicated that the printed CMNP or the eventual PMNP, subjected to post-fabrication treatment, were non-cytotoxic to the human skin cells.

### Statistical model for prediction of optimal microneedle geometry

A logistic model was implemented to study the relationship between the MN mechanical strength and microneedle geometry. Estimated coefficients for this model are  $-0.0011$ ,  $-0.0025$ ,  $-0.0036$ , and  $0.0039$  for MN curvature, interspacing, length, and tip diameter respectively. Among them, MN length with a p-value of 0.033 is significant and can help to explain the variation of the MN mechanical strength. Interspacing with a p-value of 0.13 can moderately help to explain the variance of the response variable. MN curvature and tip diameter with p-values of 0.67 and 0.68, respectively, are not significant and based on our experiments do not help for prediction of MN mechanical strength (figure 6).

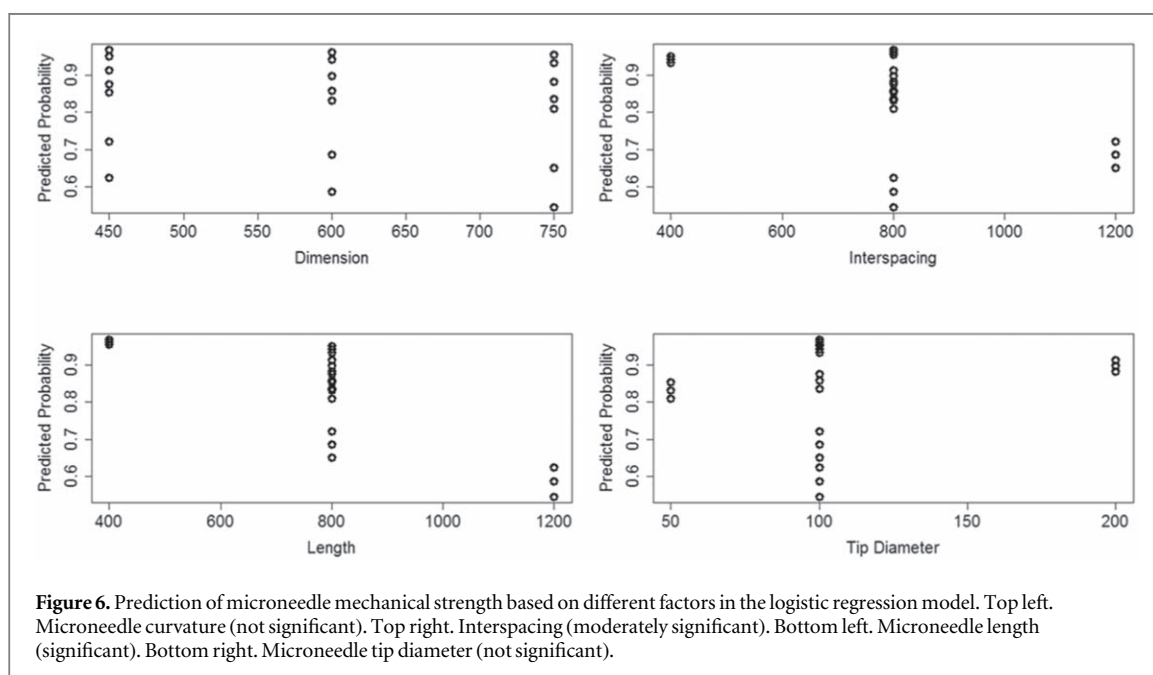
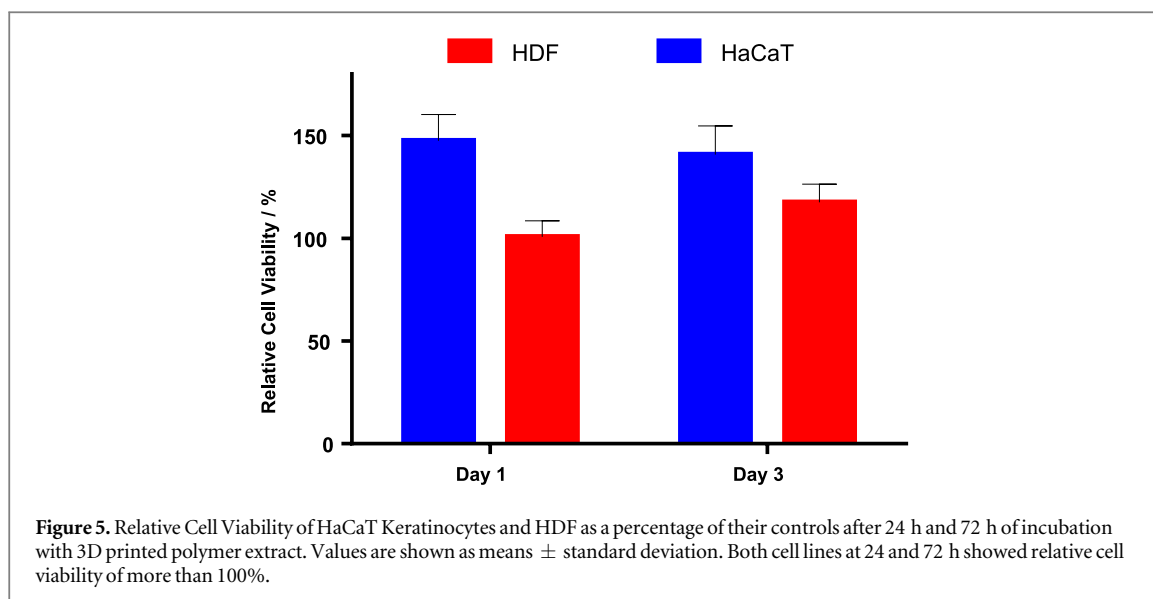
Figure 7 demonstrates the clustering results using MN geometry and mechanical strength. As we can observe in this figure, there are four clusters (one to four) that can be considered as two overlapping pairs.



First pair contains clusters one and four, and the second pair contains clusters two and three. Each number in figure 7 represents an experiment and its associated feature vector, i.e., a specific combination of parameter values for MN geometry and obtained MN mechanical strength.

The feature sets (a set of feature vectors) are shown tables S1 to S4 (supplementary information). The range of values for MN mechanical strength in each cluster along with associated range of values for MN

geometry is shown in table S5. We computed the average MN mechanical strength as well as standard error of MN mechanical strength for each cluster. As we can see, cluster one has the highest average mechanical strength of 92%, followed by cluster four with the average mechanical strength of 88.4%, while group two has the least average mechanical strength of 59%. Moreover, cluster one has the least standard error of 5.9% among all four clusters (5.9%, 10.1%, 10.3%, and 6.3% for clusters 1 to 4, respectively). The results

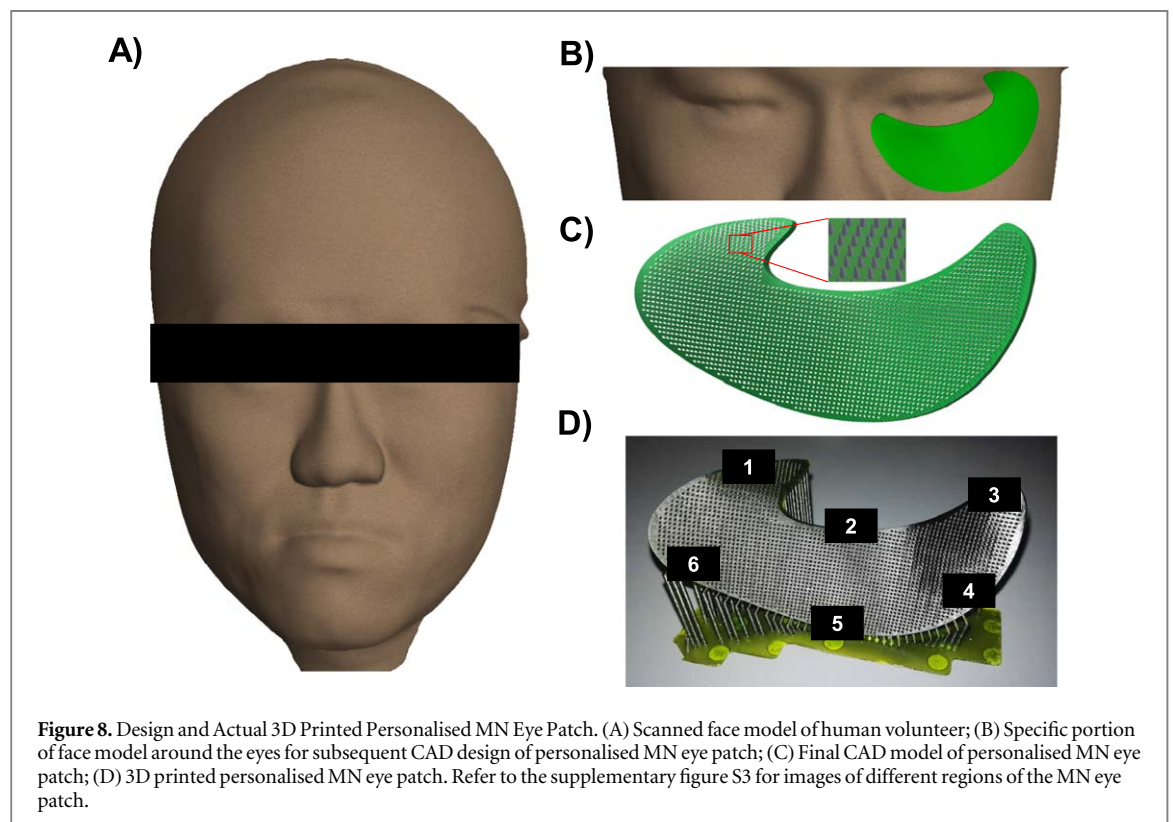
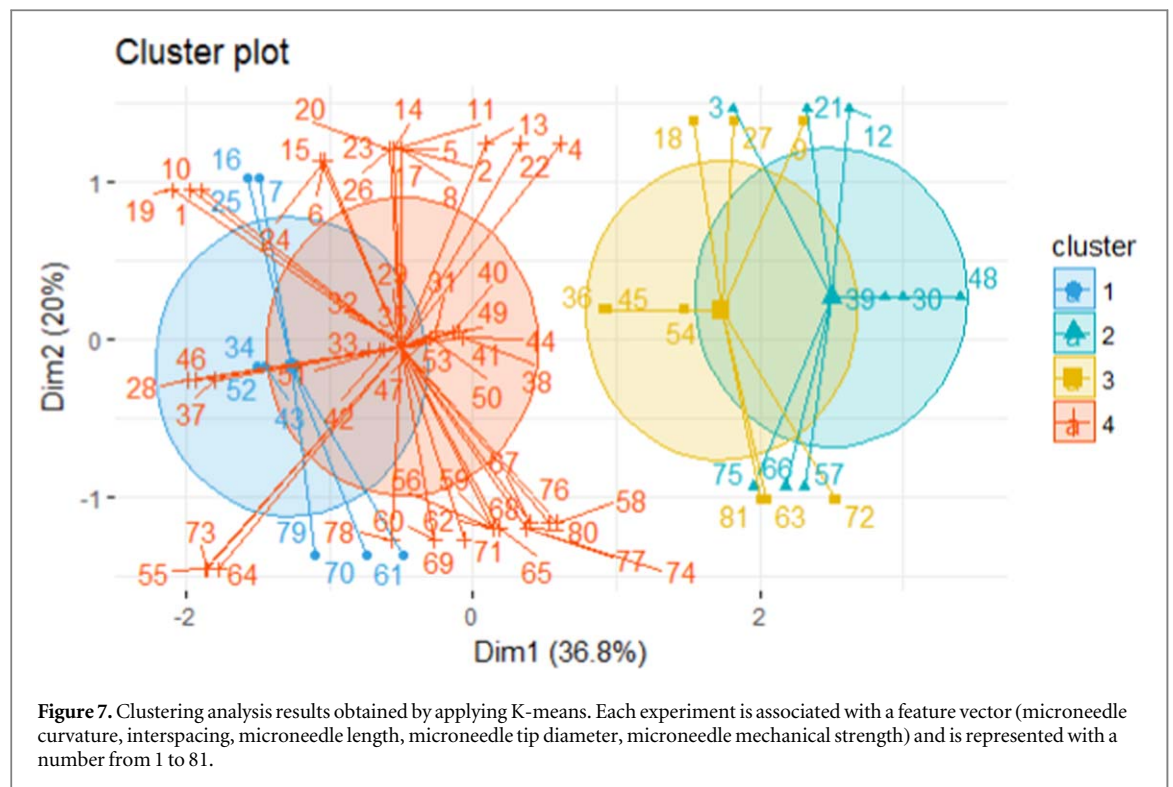


indicate that feature set associated with cluster one provides the optimal MN mechanical strength.

Next, we extracted the features for optimal microneedle mechanical strength. Table S5 shows that the curvature is not an informative feature, since it does not have a single value and feature vectors associated with cluster one covered all possible values of this feature. However, interspacing, length, and diameter have single value among all feature vectors in cluster one and the unique combination of interspacing = 400  $\mu\text{m}$ , length = 800  $\mu\text{m}$ , and diameter = 100  $\mu\text{m}$  provides the maximum average MN mechanical strength. The clustering results are consistent with the results obtained by the proposed logistic regression model.

### Design and fabrication of PMNP

A combined evaluation of mechanical strength and skin penetration efficiency data concluded that MN geometry with length of 800  $\mu\text{m}$ , tip diameter of 100  $\mu\text{m}$ , interspacing of 800  $\mu\text{m}$  and base diameter of 400  $\mu\text{m}$  was the most optimal MN geometry for all curvatures due to its good balance of both mechanical strength and skin penetration efficiency. Therefore, this combination of MN geometry was superimposed onto the PMNP and fabricated (figure 8) for subsequent characterisation and *in vitro* skin permeation study. The 3D-printed PMNP measures 65 mm (length)  $\times$  35 mm (width)  $\times$  25 mm (height) with 2465 MNs embedded.



### Histological examination of PMNP treated human cadaver skin

Histological sections with H&E staining are illustrated in figure 9 specifically with the MN-punctured pores highlighted in red. Within the punctured pores, a breakage in the continuous stratum corneum and viable epidermal layer was observed which indicated

successful penetration of the MNs through the outermost layer of the skin. Depth of penetration, estimated based on measurements of the microscope images, demonstrated a significantly ( $p$ -value  $< 0.01$ ) deeper penetration achieved by the PMNP, compared to FMNP. Intact skin had no visible punctured pores.

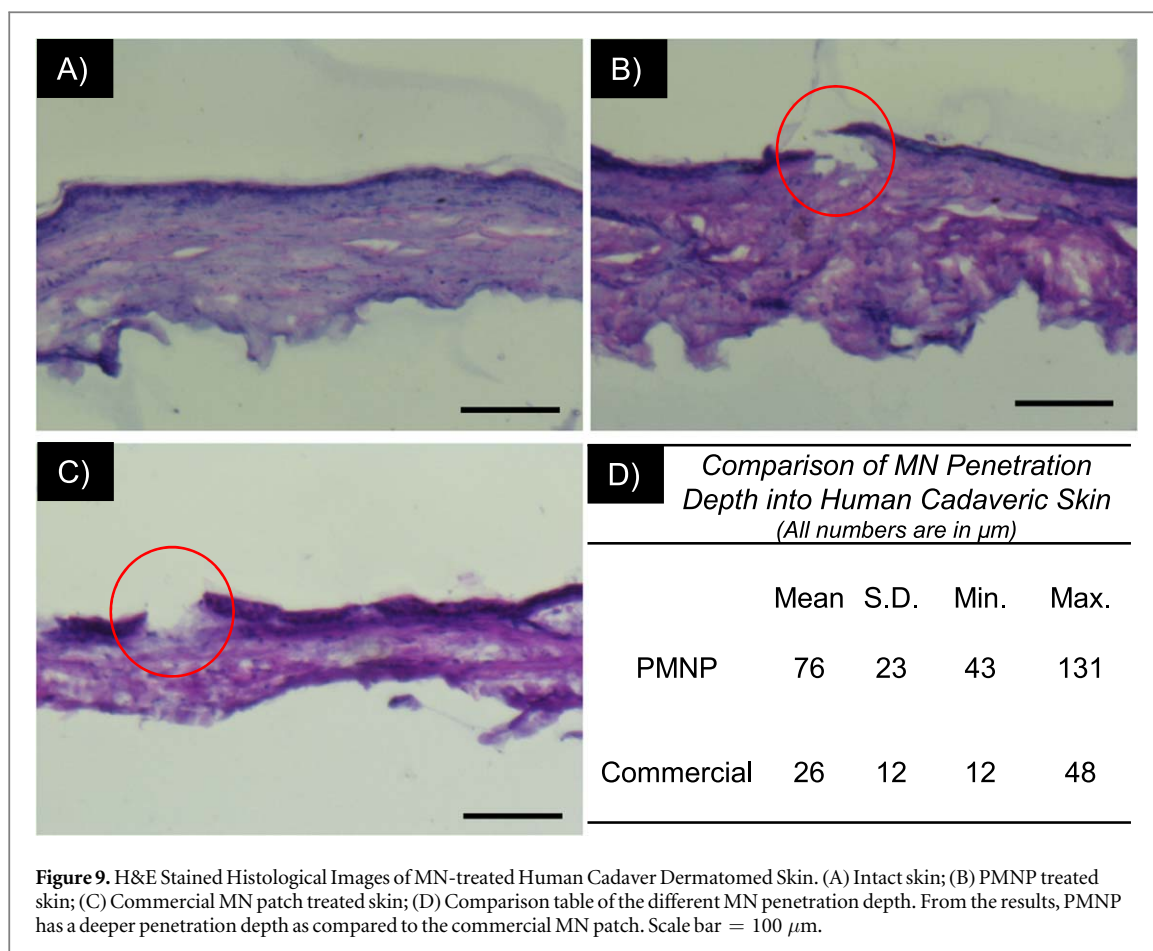


**Figure 9.** H&E Stained Histological Images of MN-treated Human Cadaver Dermatomed Skin. (A) Intact skin; (B) PMNP treated skin; (C) Commercial MN patch treated skin; (D) Comparison table of the different MN penetration depth. From the results, PMNP has a deeper penetration depth as compared to the commercial MN patch. Scale bar = 100  $\mu\text{m}$ .

#### ***In vitro* skin permeation of calcein dye through human cadaver dermatomed skin**

Calcein dye has a molecular weight of 622.55 Da and a  $\log P$  of  $-3.1$  and therefore can be used as a suitable surrogate for AHP-3. Under confocal microscope, a green fluorescence was observed at areas permeated with Calcein dye. Referring to figure 10, the approximate depth of penetration for the intact skin is  $\sim 220 \mu\text{m}$ ; FMNP  $\sim 480 \mu\text{m}$  and PMNP  $\sim 750 \mu\text{m}$ . There was no visible green fluorescence for the intact skin without calcein.

#### ***In vitro* skin permeation of AHP-3, through human cadaver dermatomed skin**

As illustrated in figure 11(A), comparing to FMNP treatment, commercial AHP-3 patch and intact skin, enhanced cumulative permeation of AHP-3 across human cadaver skin was observed for PMNP treatment at the end of a 24 h time period ( $\sim 90\text{X}$  higher compared to intact skin;  $\sim 45\text{X}$  higher than FMNP treatment). Significantly higher amount of AHP-3 was permeated through the skin at all the time points sampled for PMNP treatment, as compared to all other arms. While not as effective as PMNP treatment, a  $\sim 6\text{X}$  higher amount of permeated AHP-3 was observed at the end of 24 h for FMNP treatment, as compared to intact skin. There was no detectable amount of permeated AHP-3 for the commercial AHP-3 arm, throughout the 24 h period. Comparing

the amount of AHP-3 present within the skin at the end of 24 h (figure 11(B)), there were no significant differences between all treatment arms, except for PMNP treated skin and the commercial AHP-3 patch (without MN).

### **Discussion**

To our knowledge, this is the first study to provide an insight into the relationship between MN geometry on curved patches and its adequacy for transdermal drug delivery. In view of increasing acknowledgement that a flat MN patch is unable to achieve optimal drug delivery through the undulating human skin [19, 20], this information will be of great interest to the research and pharmaceutical industrial community. Subsequently, using the optimised MN geometry, a PMNP was fabricated and has demonstrated an enhanced delivery of AHP-3 up to  $\sim 90\text{X}$  higher as compared to intact skin and  $\sim 45\text{X}$  higher as compared to a commercially available FMNP.

From this optimisation study, it can be concluded that the general principle of geometrical effects on mechanical strength and skin penetration efficiency for curved MN patch follow that of flat patch [27, 36–39]. Firstly, a decrease in mechanical strength with increasing MN length was observed across all curvatures. This is a similar trend to the relationship in flat

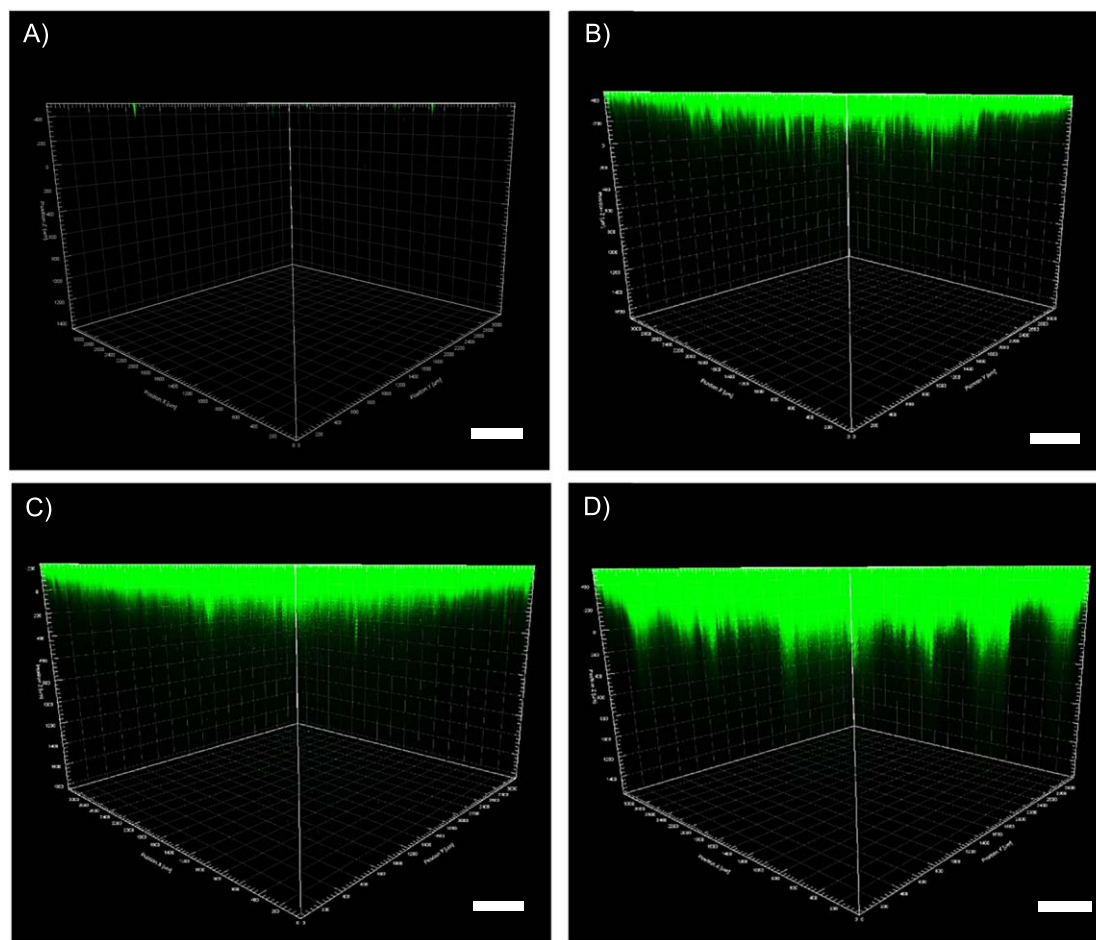
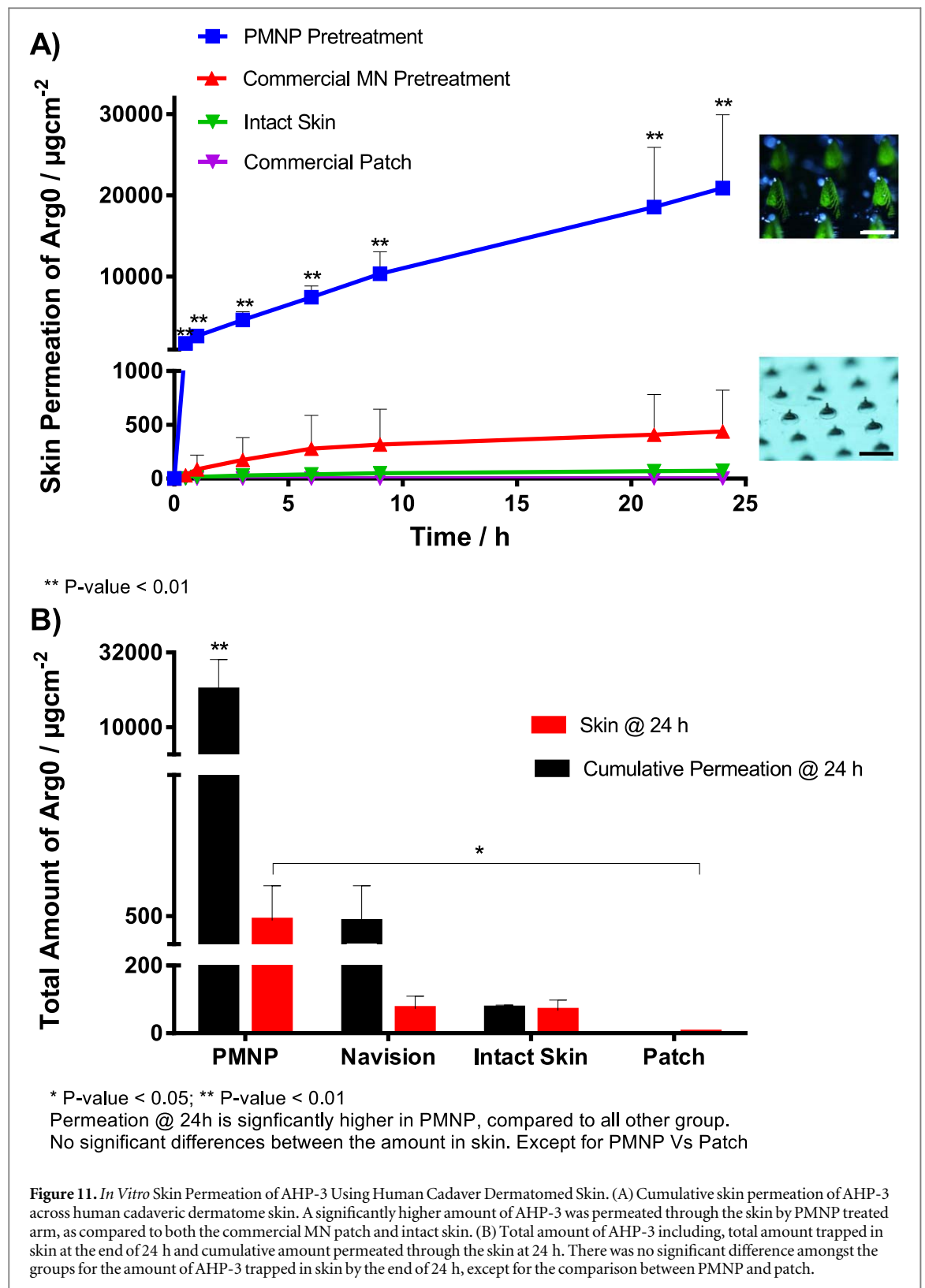


**Figure 10.** 3D Constructed Confocal Images for the *In Vitro* Skin Permeation of Calcein Dye, after 18 h, using Human Cadaver Dermatomed Skin. (A) Blank; (B) Intact skin; (C) Pre-treatment with commercial MN patch; (D) Pre-treatment with personalised microneedle patch. The green colour represents the amount of calcein in the skin. In 18 h, pre-treatment with PMNP allowed the permeation of the highest amount of calcein through the skin, followed by FMNP and finally intact skin. Scale bar = 500  $\mu\text{m}$ .

MN and can be attributed to increased shaft weakness with thinner MN structure which tends to fracture more easily upon force application. However, excessive increment in length is unfavourable due to the formation of weaker MNs with poorer penetration, as reflected by the MN length of 1200  $\mu\text{m}$  having weaker penetration through skin than 800  $\mu\text{m}$ . This may be possibly due to MN breakage before penetration given its poor strength. Secondly, a sharper MN demonstrated a higher skin penetration efficiency. A tip diameter of 200  $\mu\text{m}$  has the least penetration efficiency due to reduced MN sharpness and therefore, its ability to pierce through skin. On the other hand, both MN with tip diameters of 50  $\mu\text{m}$  and 100  $\mu\text{m}$  demonstrated higher but had no significantly higher skin penetration efficiency as compared to MN with tip diameter of 200  $\mu\text{m}$ . This may be due to increased fracture for 50  $\mu\text{m}$  possibly before penetration even though it was sharper and expected to have better penetration efficiency. Lastly, a decrease in mechanical strength with increasing MN interspacing from 400  $\mu\text{m}$  to 1200  $\mu\text{m}$  for all curvatures was observed.

This is likely due to increasing force subjected to each MN with decreasing density of the patch. Despite having poor mechanical strength, interspacing of 1200  $\mu\text{m}$  for all curvatures has higher skin penetrability as compared to that of 400  $\mu\text{m}$  and 800  $\mu\text{m}$ . This is likely due to a reduction in patch density resulting in a penetrating force exerted by each MN for skin penetration, as reported by Olatunji *et al* [40].

For successful transdermal delivery, it is crucial to consider both mechanical strength and skin penetration efficiency when determining the optimal MN geometry for each curvature of CMNP. Figure 4 demonstrated that differences exist in either mechanical strength or skin penetration efficiency for all MN lengths and interspacing across all curvatures. However, tip diameter seemed to contribute less in affecting mechanical strength and skin penetrability across all curvatures because of limited statistical differences between the various tip diameters. Therefore, it is suggested that more weight can be placed on deciding between different lengths and interspacing, as compared to tip diameter when fabricating CMNPs. This



similar trend can be concluded in the statistical analysis shown in figure 6.

The results in figure 7 illustrates the clustering analysis of the optimisation data (mechanical strength) obtained by applying K-means. From the statistical analysis in figure 6, we understand the significance of the individual factors in affecting the mechanical strength of the microneedle. However, the interaction

of these various factors together is still unknown. Clustering analysis of these optimisation data allows us to group the various parameter combination by their outcome measurement of the mechanical strength.

The results show that there are mainly 4 clusters of mechanical strengths, with two overlapping pairs. By analysing the different parameter combinations

within each clusters, we would be able to identify the optimal parameter combination for the best mechanical strength. In this case, Cluster 1 has the highest mechanical strength or percentage of MN left intact. From analysing the parameter combinations in Cluster 1, the optimal MN parameter combination is that of 800  $\mu\text{m}$  MN length, 100  $\mu\text{m}$  tip diameter, 400  $\mu\text{m}$  interspacing. This clustering analysis would be useful for subsequent optimisation of MN geometry with a different material.

However, mechanical strength alone may be insufficient and more complex clustering analysis may be required to take into account of skin penetration efficiency. In our case, we have selected the combination of 800  $\mu\text{m}$  MN length, 100  $\mu\text{m}$  tip diameter and an interspacing of 800  $\mu\text{m}$  for all curvatures. This parameter combination belongs to Cluster 4, which overlaps with Cluster 1 and can also be considered as a cluster with good mechanical strength. The decision took into account of both the mechanical strength and also skin penetration efficiency.

Interestingly, most MN geometries of the intermediate curvature exhibited better skin penetrability as compared to the sharp and gentle curvatures. MNs are subjected to shear and axial forces when compressed onto the skin surface [41]. Therefore, MNs of intermediate curvature are possibly less susceptible to each of these forces when applied to the skin, thereby having enhanced penetration efficiency. For CMNPs with sharp curvature, MNs on the sides may experience tremendous shear fracture force during application, leading to significant breakage before penetration. On the other hand, MNs on CMNPs with gentle curvature are subjected to increased axial fracture force which facilitates breakage since most MNs are punctured almost perpendicularly to the skin surface, resulting in decreased skin penetration.

Initially, it was hypothesized that each curvature will have its own optimized MN geometry due to variable MN arrangement in space, leading to distinct interactions between MN and surface used during mechanical strength or skin penetration efficiency testing. However, the results demonstrated that all three curvatures have the same optimized MN geometry. While this may be the inherent truth, some limitations of this study could have contributed to the absence of different optimized MN geometry for each curvature. Firstly, the viscoelastic property of porcine cadaver skin used for penetration study prevents reproducible MN penetration and affects insertion behaviour, leading to possible discrepancies in results obtained [42]. Secondly, limited MN dimensions were studied and may be insufficient to unravel the actual phenomenon. Moreover, smaller tip diameters cannot be studied due to limited printing resolution of DLP, but, this may be possible using other methods such as two-photon polymerization 3D printers [36]. Although MNs with smaller tip diameters have weaker mechanical strength, the insertion force required to overcome resistance of skin for penetration is also much

reduced, leading to decreased fractures and increased penetrability instead [39]. Hence, significant differences between different tip diameters, which is absent in this study, may be observed. Therefore, further research could be done to adequately elucidate the relationship between MN geometry and varying curvatures of MN patch.

At the end of the optimisation phase of this project, the best parameter combinations for the MN was identified to be MN length of 800  $\mu\text{m}$ , tip diameter of 100  $\mu\text{m}$ , interspacing of 800  $\mu\text{m}$  and base diameter of 400  $\mu\text{m}$ , regardless of the degree of curved surfaces. To validate this set of parameters, we fabricated a PMNP using a face CAD model of a human volunteer and compared it against a commercially available flexible microneedle eye patch. Based on our results in figure 8 and the subsequent figures, it was demonstrated that our PMNP performed better than the flexible flat microneedle eye patch on an undulating surface, such as the periorbital region around the eyes. In both the depth of skin penetration and cumulative amount of small peptide that permeated through the skin, our PMNP is significantly better than that of the flexible flat microneedle eye patch.

Specifically, *in vitro* skin permeation study using both Calcein and AHP-3 (figures 10, 11) demonstrated a significantly enhanced transdermal delivery potential of PMNP, as compared to intact skin ( $\sim 90\text{X}$  higher) or a commercially available FMNP ( $\sim 45\text{X}$  higher). The enhanced rate of transdermal delivery for hydrophilic macromolecules such as AHP-3 is consistent or better than published literature, as compared to delivery of other peptides using microneedles [43]. This could be attributed to increased skin penetration due to a complementary fitting of PMNP to the skin surface during application, as compared to using a flat MN patch [19]. Also, micro-channels created by MNs might have provided a direct passage for permeation of hydrophilic molecules like AHP-3, as compared to intact skin [16]. Typically, MN patches are small in surface area ( $\sim 1\text{--}2\text{ cm}^2$ ) and only suited for delivery of potent drugs. In this study, we demonstrated the fabrication and use of a large personalised MN patch to deliver peptides up to  $\sim 90\text{X}$  the usual amount. The use of handheld 3D scanners and CAD software also demonstrated a convenience in developing PMNP which can be used in future applications such as wearable devices for smart delivery of drugs.

## Conclusion

Physical characterization of MN geometry was conducted for CMNPs with varying curvatures to evaluate the relationship between different MN dimensions and their effect on mechanical strength and skin penetration efficiency. From the results obtained, an optimized MN geometry was determined. Next, *in vitro* skin permeation results via 'poke and patch'

method demonstrated that a PMNP provided enhanced delivery of AHP-3 through human cadaver skin, as compared to FMNP and intact skin. Together, increased knowledge about MN geometry selection for curved patches, advancements in 3DP technology and availability of software such as Materialize Mimics® [44, 45], which enables conversion of medical imaging scans to CAD models, provide a viable approach for PMNP fabrication to enhance transdermal delivery of AHP-3 for anti-wrinkle therapy in the future.

## Acknowledgments

A Singapore National additive manufacturing innovation cluster (NAMIC) project 2016011 and a Singapore Ministry of Education (MOE) Academic Research Fund (AcRF) Tier 1 grant (R148-000-224-112).

## Conflict of interest

The authors declare no conflict of interest.

## ORCID iDs

Lifeng Kang  <https://orcid.org/0000-0002-1676-7607>

## References

- [1] Manriquez J J, Majerson Gringberg D and Nicklas Diaz C 2008 Wrinkles *BMJ Clinical Evidence* **2008** 1711
- [2] Ganceviciene R, Liakou A I, Theodoridis A, Makrantonaki E and Zouboulis C C 2012 Skin anti-aging strategies *Dermato-endocrinology* **4** 308–19
- [3] Gupta M and Gupta A 1996 Photodamaged skin and quality of life: Reasons for therapy *J. Dermatologic. Treat.* **7** 261–4
- [4] Blanes-Mira C, Clemente J, Jodas G, Gil A, Fernandez-Ballester G, Ponsati B, Gutierrez L, Perez-Paya E and Ferrer-Montiel A 2002 A synthetic hexapeptide (Argireline) with antiwrinkle activity *Int. J. Cosmet. Sci.* **24** 303
- [5] Yamauchi P S and Lowe N J 2004 Botulinum toxin types A and B: comparison of efficacy, duration, and dose-ranging studies for the treatment of facial rhytides and hyperhidrosis *Clinics in Dermatology* **22** 34–9
- [6] Lim S H, Sun Y, Thiruvallur Madanagopal T, Rosa V and Kang L 2018 Enhanced skin permeation of anti-wrinkle peptides via molecular modification *Sci. Rep.* **8** 1596
- [7] Lupo M P and Cole A L 2007 Cosmeceutical peptides *Dermatologic Therapy* **20** 343
- [8] Wang Y, Wang M, Xiao S, Pan P, Li P and Huo J 2013 The anti-wrinkle efficacy of argireline, a synthetic hexapeptide, in Chinese subjects: a randomized, placebo-controlled study *Am. J. Clin. Dermatology* **14** 147–53
- [9] Kraeling M E, Zhou W, Wang P and Oguniola O A 2015 *In vitro* skin penetration of acetyl hexapeptide-8 from a cosmetic formulation *Cutaneous and Ocular Toxicology* **34** 46
- [10] Hoppel M, Reznicek G, Kahlig H, Kotisch H, Resch G P and Valenta C 2015 Topical delivery of acetyl hexapeptide-8 from different emulsions: influence of emulsion composition and internal structure *Eur. J. Pharm. Sci.* **68** 27
- [11] Ruiz M A, Clares B, Morales M E, Cazalla S and Gallardo V 2007 Preparation and stability of cosmetic formulations with an anti-aging peptide *J. Cosmet. Sci.* **58** 157–71
- [12] Larraneta E, Moore J, Vicente-Perez E M, Gonzalez-Vazquez P, Lutton R, Woolfson A D and Donnelly R F 2014 A proposed model membrane and test method for microneedle insertion studies *Int. J. Pharm.* **472** 65
- [13] Prausnitz M R and Langer R 2008 Transdermal drug delivery *Nat. Biotechnol.* **26** 1261
- [14] Kathuria H, Kochhar J S, Fong M H, Hashimoto M, Iliescu C, Yu H and Kang L 2015 Polymeric microneedle array fabrication by photolithography *J. Vis. Exp.* **e52914**
- [15] Ita K 2015 Transdermal delivery of drugs with microneedles-potential and challenges *Pharmaceutics* **7** 90–105
- [16] Larrañeta E, Lutton R E M, Woolfson A D and Donnelly R F 2016 Microneedle arrays as transdermal and intradermal drug delivery systems: materials science, manufacture and commercial development *Mater. Sci. Eng.: R: Reports* **104** 1–32
- [17] Li H, Low Y S, Chong H P, Zin M T, Lee C Y, Li B, Leolukman M and Kang L 2015 Microneedle-mediated delivery of copper peptide through skin *Pharm. Res.* **32** 2678–89
- [18] Choi C K, Kim J B, Jang E H, Youn Y N and Ryu W H 2012 Curved biodegradable microneedles for vascular drug delivery *Small* **8** 2483–8
- [19] Lim S H, Ng J Y and Kang L 2017 Three-dimensional printing of a microneedle array on personalized curved surfaces for dual-pronged treatment of trigger finger *Biofabrication* **9** 015010
- [20] Lahiji S F, Dangol M and Jung H 2015 A patchless dissolving microneedle delivery system enabling rapid and efficient transdermal drug delivery *Sci. Rep.* **5** 7914
- [21] Zhang P, Dalton C and Jullien G A 2009 Design and fabrication of MEMS-based microneedle arrays for medical applications *Microsyst. Technol.* **15** 1073
- [22] Kim M, Kim T, Kim D S and Chung W K 2015 Curved microneedle array-based sEMG electrode for robust long-term measurements and high selectivity *Sensors* **15** 16265
- [23] Cai B, Xia W, Bredenberg S, Li H and Engqvist H 2015 Bioceramic microneedles with flexible and self-swelling substrate *Eur. J. Pharm. Biopharm.* **94** 404–10
- [24] Rajabi M, Roxhed N, Shafagh R Z, Haraldson T, Fischer A C, Wijngaart W V, Stemme G and Niklaus F 2016 Flexible and stretchable microneedle patches with integrated rigid stainless steel microneedles for transdermal biointerfacing *PLoS One* **11** e0166330
- [25] Kathuria H, Li H, Pan J, Lim S H, Kochhar J S, Wu C and Kang L 2016 Large size microneedle patch to deliver lidocaine through skin *Pharm. Res.* **33** 2653
- [26] Kochhar J S, Zou S, Chan S Y and Kang L 2012 Protein encapsulation in polymeric microneedles by photolithography *Int. J. Nanomed.* **7** 3143–54
- [27] Kochhar J S, Goh W J, Chan S Y and Kang L 2013 A simple method of microneedle array fabrication for transdermal drug delivery *Drug Dev. Ind. Pharm.* **39** 299–309
- [28] Matsuda T and Mizutani M 2002 Liquid acrylate-encapped biodegradable poly(epsilon-caprolactone-co-trimethylene carbonate). II. Computer-aided stereolithographic microarchitectural surface photoconstructs *J. Biomed. Mater. Res.* **62** 395–403
- [29] Recommended printing parameters: exposure time, lifting height, & lifting speed (<https://kudo3d.com>) (Accessed 27 March 2020)
- [30] Oskui S M, Diamante G, Liao C, Shi W, Gan J, Schlenk D and Grover W H 2016 Assessing and reducing the toxicity of 3D-printed parts *Environmental Science & Technology Letters* **3** 1
- [31] Kochhar J S, Anbalagan P, Shelar S B, Neo J K, Iliescu C and Kang L 2014 Direct microneedle array fabrication off a photomask to deliver collagen through skin *Pharm. Res.* **31** 1724
- [32] Kochhar J S, Lim W X, Zou S, Foo W Y, Pan J and Kang L 2013 Microneedle integrated transdermal patch for fast onset and sustained delivery of lidocaine *Mol. Pharmaceutics* **10** 4272

- [33] Chu L Y, Choi S O and Prausnitz M R 2010 Fabrication of dissolving polymer microneedles for controlled drug encapsulation and delivery: bubble and pedestal microneedle designs *J. Pharm. Sci.* **99** 4228–38
- [34] Larrañeta E, Moore J, Vicente-Pérez E M, González-Vázquez P, Lutton R, Woolfson A D and Donnelly R F 2014 A proposed model membrane and test method for microneedle insertion studies *Int. J. Pharm.* **472** 65–73
- [35] Development of self-dissolving microneedles consisting of hyaluronic acid as an anti-wrinkle treatment (<https://shiseidogroup.com/rd/ifsc/19.html>) (Accessed 27 March 2020)
- [36] Gittard S D, Chen B, Xu H, Ovsianikov A, Chichkov B N, Monteiro-Riviere N A and Narayan R J 2013 The effects of geometry on skin penetration and failure of polymer microneedles *J. Adhes. Sci. Technol.* **27** 227–43
- [37] Yan G, Warner K S, Zhang J, Sharma S and Gale B K 2010 Evaluation needle length and density of microneedle arrays in the pretreatment of skin for transdermal drug delivery *Int. J. Pharm.* **391** 7–12
- [38] Nguyen H X and Banga A K 2015 Enhanced skin delivery of vismodegib by microneedle treatment *Drug Deliv. Transl. Res.* **5** 407
- [39] Davis S P, Landis B J, Adams Z H, Allen M G and Prausnitz M R 2004 Insertion of microneedles into skin: measurement and prediction of insertion force and needle fracture force *J. Biomech.* **37** 1155
- [40] Olatunji O, Das D B, Garland M J, Belaid L and Donnelly R F 2013 Influence of array interspacing on the force required for successful microneedle skin penetration: theoretical and practical approaches *J. Pharm. Sci.* **102** 1209
- [41] Khanna P, Luongo K, Strom J A and Bhansali S 2010 Axial and shear fracture strength evaluation of silicon microneedles *Microsyst. Technol.* **16** 973
- [42] Donnelly R F, Garland M J, Morrow D I, Migalska K, Singh T R, Majithiya R and Woolfson A D 2010 Optical coherence tomography is a valuable tool in the study of the effects of microneedle geometry on skin penetration characteristics and in-skin dissolution *J. Controlled Release* **147** 333
- [43] Mohammed Y H, Yamada M, Lin L L, Grice J E, Roberts M S, Raphael A P, Benson H A and Prow T W 2014 Microneedle enhanced delivery of cosmeceutically relevant peptides in human skin *PLoS One* **9** e101956
- [44] Materialize Mimics (<http://materialise.com/en/medical/software/mimics>) (Accessed 27 March 2020)
- [45] Kim G B *et al* 2016 Three-dimensional printing: basic principles and applications in medicine and radiology *Korean Journal of Radiology* **17** 182